A Volcano Rekindled: The Renewed Eruption of Mount St. Helens, 2004–2006
Edited by David R. Sherrod, William E. Scott, and Peter H. Stauffer
U.S. Geological Survey Professional Paper 1750, 2008

Chapter 12

Extrusion Rate of the Mount St. Helens Lava Dome Estimated from Terrestrial Imagery, November 2004–December 2005

By Jon J. Major[1], Cole G. Kingsbury[1], Michael P. Poland[2], and Richard G. LaHusen[1]

Abstract

Oblique, terrestrial imagery from a single, fixed-position camera was used to estimate linear extrusion rates during sustained exogenous growth of the Mount St. Helens lava dome from November 2004 through December 2005. During that 14-month period, extrusion rates declined logarithmically from about 8–10 m/d to about 2 m/d. The overall ebbing of effusive output was punctuated, however, by episodes of fluctuating extrusion rates that varied on scales of days to weeks. The overall decline of effusive output and finer scale rate fluctuations correlated approximately with trends in seismicity and deformation. Those correlations portray an extrusion that underwent episodic, broad-scale stick-slip behavior superposed on the finer scale, smaller magnitude stick-slip behavior that has been hypothesized by other researchers to correlate with repetitive, nearly periodic shallow earthquakes.

Introduction

Aerial and terrestrial photography are effective ways of monitoring morphological changes that occur during volcanic eruptions (see, for example, Zlotnicki and others, 1990; Yamashina and others, 1999; Baldi and others, 2000, 2005; Honda and Nagai, 2002; Herd and others, 2005; Thompson and Schilling, 2007; Poland and others, this volume, chap. 11; Schilling and others, this volume, chap. 8). Some camera deployments and photography campaigns are aimed chiefly at monitoring volcanic activity qualitatively, whereas others endeavor to gather photographs sufficient to make quantitative (photogrammetric) measurements of static features or dynamic processes. For example, aerial photography has been used to estimate volumes of volcanic deposits and lava domes, to measure magnitudes of edifice deformation, to estimate volumetric loss during dome collapse, and to model development of volcano glaciers (for example, Moore and Albee, 1981; Jordan and Kieffer, 1981; Zlotnicki and others, 1990; Sparks and others, 1998; Schilling and others, 2004; Herd and others, 2005; Schilling and others, this volume, chap. 8). Similarly, ground-based photographs have been used to provide dynamic data of active processes, such as velocity estimates of large debris avalanches and lateral blasts (Voight, 1981), short-term (days) growth rates of lava domes (Yamashina and others, 1999), and motion of lava flows (James and others, 2006), and for geometric reconstructions of volcanic stratigraphy (Dungan and others, 2001). Commonly, stereoscopic imagery is used in such analyses, but apparent parallax caused by movement of an object in repeat photographs from a fixed position has also been exploited.

During the 2004–5 eruption of Mount St. Helens, oblique terrestrial imagery from remotely stationed cameras was one of the chief methods for monitoring the nature and pace of the eruption (Poland and others, this volume, chap. 11). Cameras were deployed principally to monitor the eruption visually without exposing scientists to unnecessary risk and to provide ancillary information on conditions in the crater (such as weather, the amount of steaming, or blowing ash) for purposes of planning field work. They were not deployed specifically for photogrammetric purposes.

Quantitative analysis of oblique terrestrial imagery commonly requires stereoscopic imagery or well-controlled nonstereoscopic imagery from multiple camera positions (Wolf and Dewitt, 2000). From October 2004 through December 2005 and beyond (Poland and others, this volume, chap. 11), however, we obtained repeat, ground-based imagery of the Mount St. Helens eruption from a single, fixed-position

[1] U.S. Geological Survey, 1300 SE Cardinal Court, Vancouver, WA 98683

[2] U.S. Geological Survey, PO Box 51, Hawaii National Park, HI 96718

camera located near the mouth of the volcano's crater. After August 2005, other ground-based cameras were located elsewhere around the volcano (Poland and others, this volume, chap. 11), but none of those provided stereoscopic imagery. In this paper, we employ a methodology for quantifying the linear extrusion rate of a growing silicic lava dome from the imagery obtained by the camera deployed near the crater mouth, summarize the results of spatial and temporal variations of dome growth and extrusion rates from November 2004 through December 2005, and compare our results with corresponding time series of seismic-energy release and local deformation measured by continuous Global Position System (GPS) receivers (Moran and others, this volume, chap. 2; LaHusen and others, this volume, chap. 16). Previously, average extrusion rates of silicic lava domes have been determined for discrete, short-lived eruptions or eruptive episodes (for example, Huppert and others, 1982; Swanson and others, 1987; Nakada and others, 1995; Sparks and others, 1998), although extrusion rates of a continuous, decadal-scale eruption have been measured by Rose (1987) and by Harris and others (2003). Demonstration of fine-scale temporal and spatial rate variation during a long-term, continuous extrusion is rare, however (for example, Sparks and others, 1998). Our data provide further insights on fine-scale behavior of sustained silicic dome growth, and they provide constraints for mathematical models that elucidate the physics of dome growth (for example, Barmin and others, 2002; Melnik and Sparks, 2005; Iverson and others, 2006; Iverson, this volume, chap. 21; Mastin and others, this volume, chap. 22).

The Sugar Bowl Camera

To photographically monitor dome growth at Mount St. Helens, we deployed a camera at the northeast end of the volcano's crater, on the Sugar Bowl lava dome, about 2.3 km from the locus of eruptive activity (fig. 1*A*). We used an Olympus 3030Z camera having a serial port (fig. 1*B*).

The camera utilizes a 1/1.8 inch solid-state sensor and has a nominal 6.5–19.5 mm focal length lens, equivalent to a 32–96 mm lens on a 35-mm camera. The camera was programmed to expose images at its maximum focal length and to record them at 1,280×960 pixels (~1.2-megapixel images). The relatively low-resolution setting was intended to permit rapid capture and transmission of images of explosions or other dynamic phenomena. Communications with the camera and transmission of images were enabled via radio through the serial port. Images were transmitted to a base-station computer located at the Mount St. Helens National Volcanic Monument's Coldwater Ridge Visitor Center, ~13 km downvalley (northwest) from the volcano. Once an image was transmitted, the camera acquired another image. The rate at which an image could be transmitted through the radio link governed the frequency of image acquisition, but in general images were acquired about every 3 minutes during daylight hours. Approximately once per hour the base-station computer transmitted an image to the Cascades Volcano Observatory. As needed, the computer could be queried to retrieve images more frequently. Periodically, all images were retrieved from the Coldwater Ridge Visitor Center.

The camera, deployed in a weatherproof housing (fig. 1*B*), began operating on October 10, 2004 (Poland and others, this volume, chap. 11). It was replaced by another camera and remounted on a fixed pipe in February 2006 and replaced again in May 2006. Owing to episodic cloud cover, ice rime, pitting of the window glass, and unit failures, usable imagery is discontinuous over the period of deployment. In this paper we focus on imagery obtained from November 2004 through December 2005, roughly the first year of the eruption that began in October 2004.

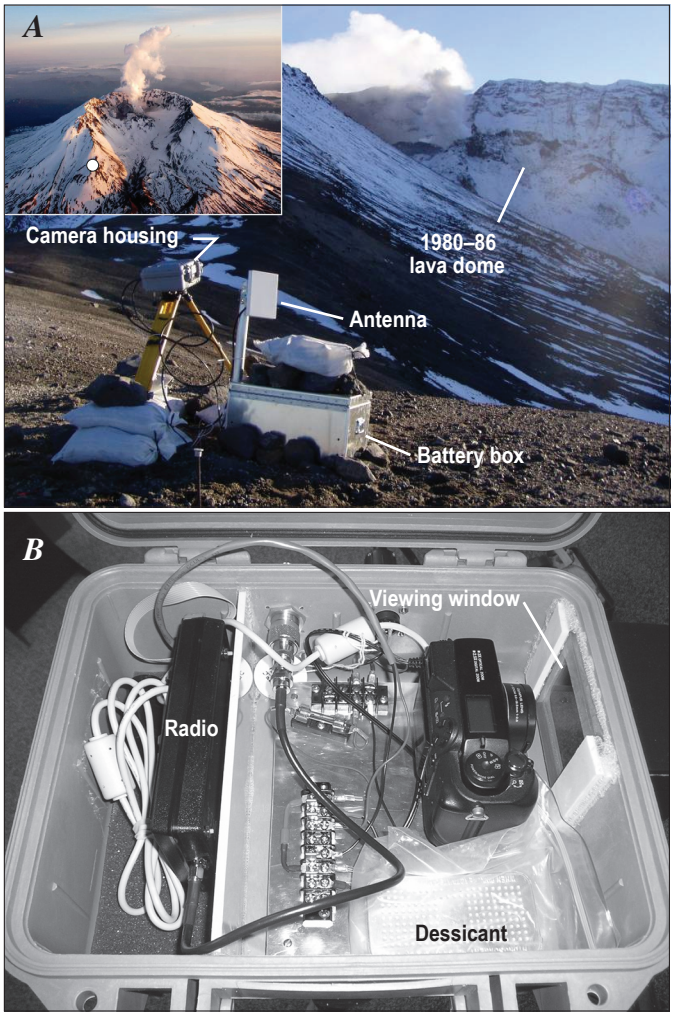

Figure 1. Photographs showing the camera system at Sugar Bowl lava dome. *A,* Deployed system at crater mouth. View is to southwest. Inset shows site location (white dot) on Sugar Bowl dome. Locus of eruptive activity is marked by emission of steam immediately to left rear of the partly snowclad 1980s lava dome. *B,* Camera and radio inside weatherproof housing.

Methodology

Theory of Terrestrial Image Analysis

The style of terrestrial imagery is defined on the basis of the orientation of the camera axis at the time of exposure. A horizontal terrestrial image is obtained when the camera axis is oriented horizontally at the time of exposure. If the camera is properly leveled before exposure, the x and z photographic axes are, respectively, oriented horizontally and vertically. Armed with precise information about camera and lens characteristics and an ability to pinpoint the optical center, or principal point, of a photograph, one can employ simple trigonometry to determine the horizontal and vertical angles between the camera axis and the rays to points in an object space (Wolf and Dewitt, 2000; fig. 2). If the camera is inclined from the horizontal, the resulting photograph is considered an oblique terrestrial image. In that case, computations of the angular differences between the camera axis, the rays to objects of interest, and a horizontal plane must account for the angle of inclination of the camera (Wolf and Dewitt, 2000).

The geometric relations among a camera's position, L, its focal length, f, the principal point of the photograph, o, the inclination angle of the camera axis, θ, and the horizontal and vertical angles to an image point are shown in figure 3. The horizontal angle, α_a, between the vertical plane containing image point a and the vertical plane containing the camera axis, Lo, is given by (Wolf and Dewitt, 2000):

$$\alpha_a = \tan^{-1}(x_a / f\sec\theta - z_a \sin\theta). \quad (1)$$

To conform to sign conventions, negative inclination angles refer to depression below, and positive inclination angles to elevation above, the horizontal (Wolf and Dewitt, 2000). In equation 1, correct algebraic signs must be applied to x_a, z_a, and θ. The vertical angle,β_a, to image point a is given by

$$\beta_a = \tan^{-1}(z_a \cos\theta / (f\sec\theta - z_a \sin\theta)\sec\alpha_a). \quad (2)$$

In equation 2, the algebraic sign of β is automatically obtained from the sign of the z_a coordinate (Wolf and Dewitt, 2000).

Although equations 1 and 2 allow determination of the horizontal and vertical angles to any image point relative to the camera axis, they represent an underdetermined system of equations with respect to quantifying horizontal or vertical distances unless some geodetic control can be established between the camera and an object of interest. Typically, control is provided by interior and exterior referenced orientations. Interior orientation includes camera

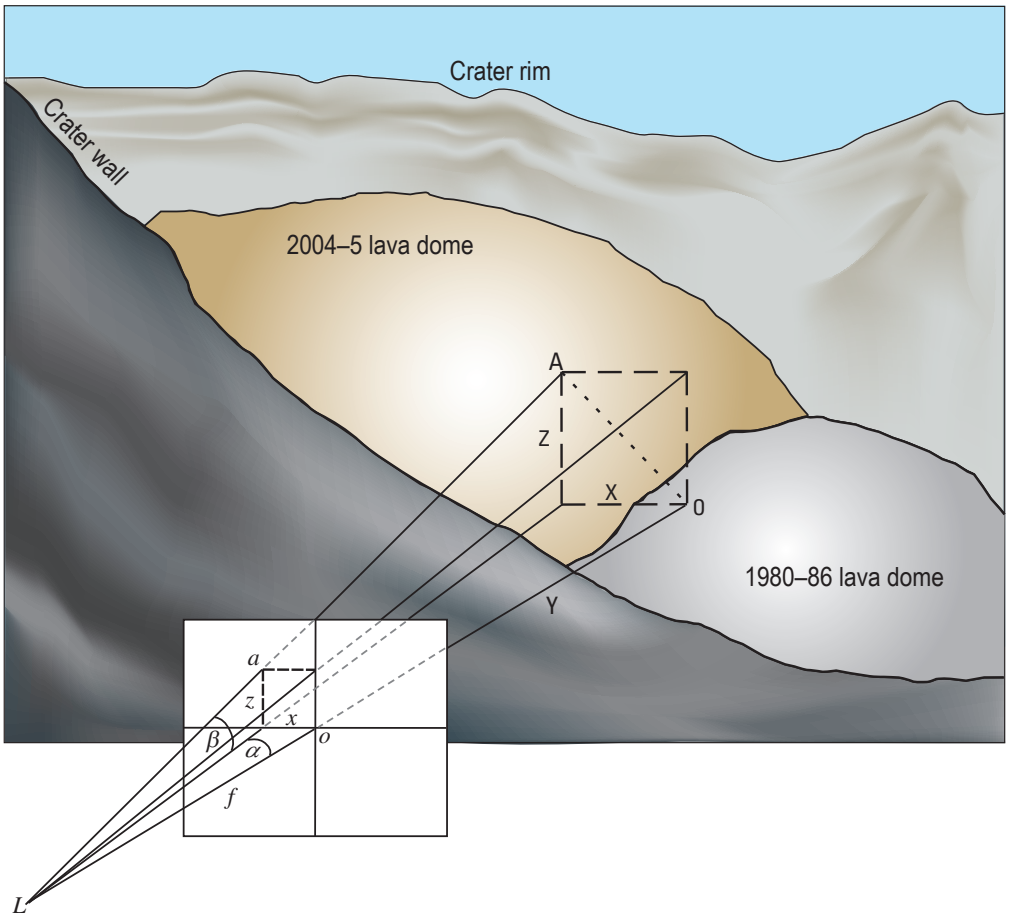

Figure 2. Diagram showing relations among optical rays from photographed objects and images projected in the focal plane for a horizontal terrestrial image. For clarity, positions of the focal plane and lens nodal point have been reversed. Focal length of the lens, f, and principal point of the image, o, are shown relative to L, the lens nodal point or position of the camera. Projections of object point, A, and the horizontal (X) and vertical (Z) distances of the object point relative to the camera axis are shown on the projected image as a, x, and z, respectively. Object distance, Y, horizontal angle, α, between the vertical plane containing the object point and the vertical plane containing the camera axis, and vertical angle, β, from a horizon line to the object point are also shown.

calibration parameters such as lens focal length, location of the image principal point, and corrections for lens distortion. Exterior orientation refers to the position and orientation of the camera with respect to a ground-based reference frame or with respect to the photographed object (Wolf and Dewitt, 2000; Molander, 2001). Orientation with respect to a ground-based reference frame is commonly accomplished by combining camera control (position and orientation) with object-space control (through established control points within the field of view).

In the absence of sound calibration parameters, one can approximate interior orientation of a digital camera from metadata contained in an image's exchangeable image format (EXIF) file and by assuming that the principal point is at the center of the image. At maximum focal length, zoom lenses commonly have minimal distortion, even on consumer-grade cameras. Such assumptions, of course, can introduce large errors to a photogrammetric analysis.

In the absence of independently established control points, one way to establish exterior orientation of a fixed camera is by measuring the orientation and position of the camera with respect to a photographed object. For the Sugar Bowl camera, we lack rigid calibration parameters. We do, however, have empirical calibration parameters from four similar cameras. In the absence of a solid camera calibration, we used averaged parameters obtained from the calibrations of those other cameras (table 1). We imposed exterior control on the imagery by measuring the camera orientation (direction of the camera axis and angle of inclination) and its location (using GPS), and we established its position relative to the proximal part of the actively growing dome by measuring coordinates and distances between the camera and the dome on sequential digital elevation models (DEMs) (Schilling and others, this volume, chap. 8; fig. 4). By fixing the distance between the camera and the near-vent area of the dome between sequential DEMs, knowing the camera orientation, and employing averaged lens characteristics, we solved all necessary trigonometric equations and roughly quantified magnitudes and rates of dome growth.

Resolving horizontal and vertical displacement rates within the focal plane of the image provided only apparent rates of extrusion, however. Quantifying more accurate linear

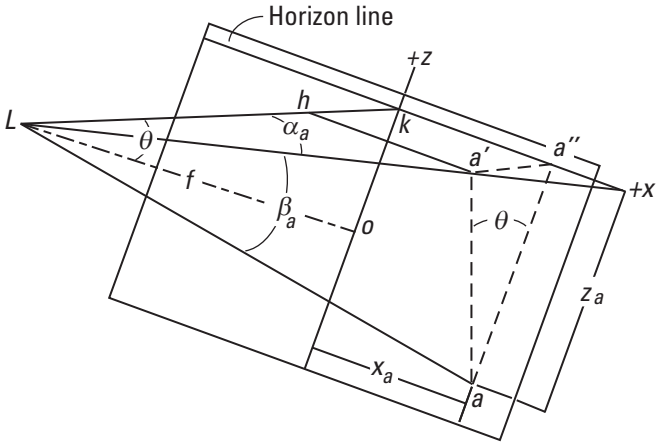

Figure 3. Diagram showing relations among optical rays from photographed objects and images projected in the focal plane of the camera for an oblique terrestrial image (slightly modified from Wolf and Dewitt, 2000; diagram copyright The McGraw-Hill Companies, Inc.). For clarity, the positions of the focal plane and lens nodal point have been reversed (see fig. 2). Focal length of the lens, *f*, principal point of the image, o, and angle of inclination of the camera axis, θ, are shown relative to *L*, the lens nodal point or position of the camera, and a horizontal line (*+x*). The projection of object point A (not shown) and its position relative to the photograph coordinate system (*+x*, *+z*) are shown on the projected image as *a*, x_a, and z_a, respectively. Line *Lk* is a horizontal line that intersects the photograph at point *k*. Line *aa´* is a vertical line, with *a´* located in a horizontal plane. Points *h* and *a*'' represent geometric projections used in the derivation of equations 1 and 2. Angles α_a and β_a are the horizontal and vertical angles of the image point, *a*, relative to horizontal and vertical axes. See Wolf and Dewitt (2000) for detailed discussions of geometric relations and derivations of equations 1 and 2.

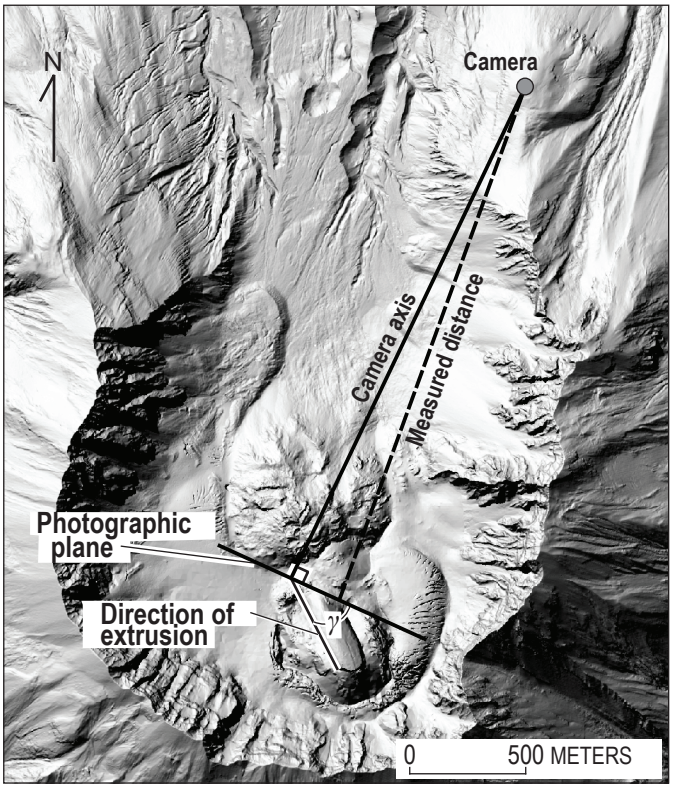

Figure 4. Digital elevation model of Mount St. Helens for February 21, 2005, showing positions of Sugar Bowl camera and 2004–5 lava dome, and relation between camera axis and obliquity of extrusion, γ. Measured distance is from camera to an identifiable feature on the dome. Trigonometric manipulation of this distance and the angular difference between that axis and the camera axis allowed computation of the distance along the camera axis.

Table 1. Camera characteristics and orientation parameters for the Sugar Bowl imagery, Mount St. Helens, Washington.

Parameter	Value
Camera characteristics	
Maximum sensor width [1]	7.76 mm
Maximum pixels at 1.2 megapixel setting	1,280 (1,280 × 960)
Field of view (at maximum focal length)	21°±1°
Resolvable pixel footprint at nominal distance to dome	~ 0.65 m
Lens characteristics	
Lens focal length (maximum) [1]	20.8 mm±1.2 mm
Lens distortion (radial) [1]	$\leq 10^{-4}$ mm
Camera orientation	
Inclination angle	7°±0.5°
Axis azimuth	207°±0.5°
Spatial measurements	
Camera location (UTM coordinates, zone 10, datum is WGS84)	5118137N, 563633E, ±10 m
Distance from camera to plane tangent to proximal dome	2,315 m ± 30 m
Obliquity of extrusion relative to focal plane	27°–53°±2°

[1] Values of these parameters represent averages obtained from empirical calibrations (using Photomodeler Pro 5) of four other Olympus C3030Z cameras.

extrusion rates of the dome required resolving trigonometric differences between the apparent direction of motion in the focal plane and the actual direction of motion. Again, by using sequential DEMs of the dome, we measured the angle of obliquity, γ, between the focal plane and the principal direction of dome growth (fig. 4). Analysis of a three-dimensional pyramid formed by the principal motion vectors (fig. 5) revealed that the angle, δ, between the vector of apparent motion in the focal plane (vector **c** in fig. 5) and the vector of actual motion (vector **V** in fig. 5) is related to the obliquity angle, γ, measured on the DEMs by

$$\delta = \tan^{-1}(R \tan \gamma), \qquad (3)$$

where R is the ratio of the horizontal motion vector (vector **b** in fig. 5) to the resolved motion vector, **c**, in the focal plane (fig. 5). From that relation, simple trigonometric relations can be solved to estimate the extrusion rate in the direction of dome growth. Our methods and analysis are, of course, subject to many possible errors (discussed below) and are limited to extrusion rates that exceed about 1 to 1.5 m/d (displacements of about 2 to 3 pixels per day; table 1). Nevertheless, they represent useful procedures for extracting quantitative information from relatively low-resolution images from a fixed position obtained from an uncalibrated (and now damaged) camera.

Tracking Distinctive Features

To estimate extrusion rates, we followed movements of distinctive features on the lava dome between selected images. These features consisted of sharp edges, intersecting fractures, fracture tips, spots, or other stable, distinctive markers that could be readily identified and that persisted through multiple images, typically from a few days to about two weeks. To begin, an initial image (November 10, 2004) was imported into graphical design software and its apparent principal point (the center of the image) identified. Coordinates of features of interest on the dome were then computed relative to that apparent principal point (fig. 6). Subsequent images (separated by roughly 24 hours when possible) were then imported and manually coregistered with the preceding image, and the positions of displaced features of interest were updated. Coordinates of distinctive features on the dome in proximity to the vent area were entered into a spreadsheet, and equations 1 and 2 solved for the employed camera parameters (table 1) and measured distances between the camera and the dome (the distance was updated with each new DEM). The solutions, along with elapsed times between photographs, provided a time series of apparent horizontal and vertical displacement rates for selected proximal points on the actively growing dome. Typical rates of apparent horizontal and vertical displacement, and standard deviations of those rates, were estimated by averaging apparent displacement rates of 3 to 10 points per image. Apparent linear extrusion rates in the focal plane were determined by resolving the averaged horizontal and vertical displacement rates, and the standard deviation errors on those averaged rates were propagated to the resolved solution using standard methods (for example, Bevington and Robinson, 1992). An average extrusion rate in the direction of dome growth was determined by resolving the average appar-

ent extrusion rate in the focal plane with respect to the angle of obliquity of extrusion.

Sources of Error

Several sources of error are inherent in a quantitative analysis of oblique imagery from the Sugar Bowl camera. A fixed source of error involves the quantification of lens characteristics, camera orientation, and spatial measurements (table 1) that affect the interior and exterior control imposed on the imagery. More random is the operator error incurred during image analysis.

Lens characteristics used in this analysis represent average values obtained from calibrations of four similar cameras. Variations of 1.2 mm about the assumed focal length (table 1) cause ±7 percent variation of the averaged apparent extrusion rates we report. Calibrated radial distortion in imagery was essentially negligible (table 1) and was thus ignored in our analyses. Repeated measurements of the inclination and azimuth of the camera housing during field visits minimized orientation error (table 1), although frequent misalignments among sequential photographs show that wind and transient snow and ice loads caused minor variations in orientation.

Spatial measurement errors revolve around accuracy of the camera location, inherent errors in the DEMs, measurement of the distance from the camera to the active extrusion, and measurement of the obliquity of the extrusion with respect to the camera axis. Replicable GPS measurements of the camera location and coordinate determinations in a GIS of selected locations on the active extrusion limit the error of the distance between the camera and the active extrusion to about ±30 m, or about 1-percent error on the measured distance (table 1). Inherent errors in the DEMs (Schilling and others, this volume, chap. 8) are small compared to other measurement errors and are thus ignored. For much of the period from November 2004 to August 2005, the dome grew along azimuths ranging from 150° to 170° (Schilling and others, this

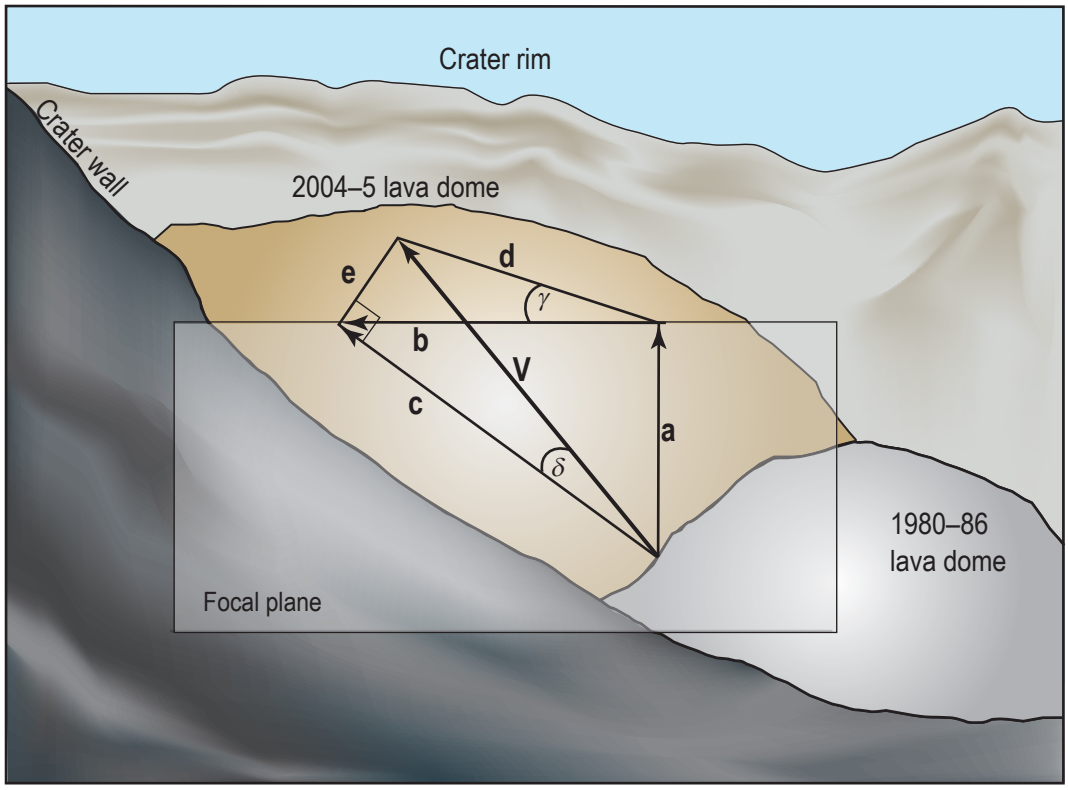

Figure 5. Diagram of a three-dimensional pyramid showing relations among the apparent vector of the average rate of motion, **c**, within a vertical plane perpendicular to the camera axis, the actual vector of extrusion, **V**, and the angle of obliquity of extrusion, γ. Triangle **abc** is oriented vertically and perpendicular to the camera axis, and triangle **ebd** is oriented orthogonally to triangle **abc** (that is, in the plane of the topographic digital elevation model). As a result, triangle **ecV** is a right triangle. Note that leg **e** is common to triangles **ecV** and **ebd**. Therefore, $\mathbf{e} = \mathbf{b} \tan\gamma = \mathbf{c} \tan\delta$. Solving this equality leads to $\tan\delta = (\mathbf{b}/\mathbf{c}) \tan\gamma$, or $\delta = \tan^{-1}(R \tan\gamma)$, where $R = \mathbf{b}/\mathbf{c}$. Thus, by measuring the angle of obliquity of extrusion, γ, on a DEM, one can employ simple trigonometry to resolve the apparent average rate of motion in the focal plane to the estimated rate of extrusion in the direction of dome growth.

volume, chap. 8; Vallance and others, this volume, chap. 9), about 30°–50° oblique to the focal plane of the camera (which had an azimuth of 117°; table 1). From about mid-August through December 2005, motion was chiefly westward (~270° azimuth), about 25°–30° oblique to the focal plane of the camera. Repeated measurements of these obliquity angles within a GIS constrained these values to within a few degrees (table 1). Errors of ±2° about the measured obliquity angles cause ±2 percent variation in the reported averaged extrusion rates.

Aside from assumptions about lens characteristics and estimates of the distance from the camera to the dome, our most critical sources of error revolve around selection of the photographic principal point, the accuracy to which sequential photographs were coregistered, and the accuracy with which moving points were identified and tracked. For purposes of the analysis reported here, the principal point to which all measurements are referenced was selected simply as the center of the first base image, and all subsequent images were coregistered to that principal point. Owing to minor variations in fields of view resulting principally from winds and snow and ice loads on the housing, the principal point of the base image was not always the principal point of subsequent images. The distinctive dome features we followed were identified at the pixel level where possible, but the relatively low resolution of the images and the sometimes challenging lighting made pixel-level identification frequently difficult. Manual identification of displaced point positions could thus be in error by a few pixels. Overall, the greatest errors in the analysis were introduced through assumptions about lens focal length and through manual image registration and feature tracking.

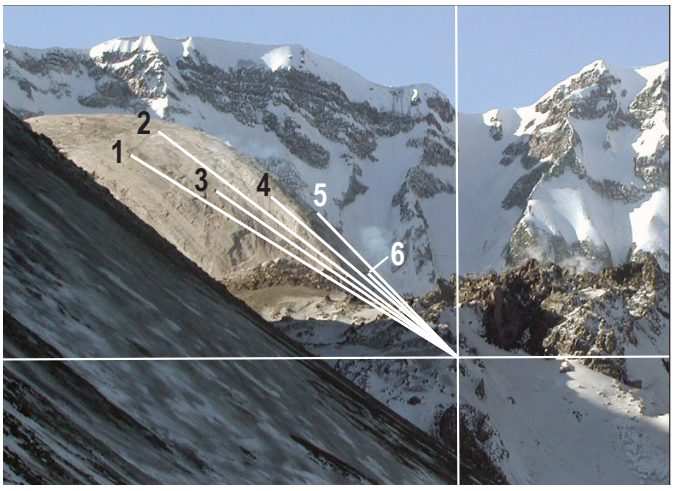

Figure 6. Example of photograph taken by the Sugar Bowl camera of the 2004–5 dome in the crater of Mount St. Helens, illustrating a distribution of points used to track motion. Because the image has been cropped, the principal point of the original photograph, which serves as the origin to which point coordinates (for example, 1 to 6) are referenced, is offset. In this image, the 2004–5 dome is about 130 m tall. Photograph taken on March 6, 2005, at 17:08:38 UTC.

Given the several sources of error that potentially affect our analysis, quantifying the cumulative error on our estimates of extrusion is a daunting task. Instead, we computed standard deviations of mean vertical and horizontal displacement rates in the focal plane from a collection of points on the proximal part of the active extrusion. Using standard practices (for example, Bevington and Robinson, 1992), we propagated the standard deviations of those mean values to the resolved extrusion rates in the focal plane and carried the propagated errors over to the resolved extrusion rates in the direction of dome growth to approximate a magnitude of error associated with our estimates of extrusion rate.

Results

Episodic growth and disintegration of several solidified lava spines characterized emplacement of the 2004–5 dome (Schilling and others, this volume, chap. 8; Vallance and others, this volume, chap. 9). Two minor spines, not visible from Sugar Bowl, breached the surface in October 2004. From late October 2004 until mid-April 2005, dome growth proceeded chiefly through emplacement and disintegration of two recumbent spines (spines 3 and 4) dubbed ‘whalebacks’ (Schilling and others, this volume, chap. 8; Vallance and others, this volume, chap. 9; fig. 7; supplemental movie in appendix 1). The character of growth changed following disintegration of spine 4 in mid-April 2005. More vertical, rather than recumbent, growth characterized spine 5 from mid-April until late July 2005 (fig. 7; supplemental movie). Following disintegration of spine 5 in late July 2005, vertical growth diminished and horizontal motion intensified as a new spine (spine 6) emerged and migrated rapidly westward. This phase of development persisted into October 2005, as a graben opened along the central part of the dome complex (see fig. 7 and supplemental movie) and growth of spine 6 became more endogenous. From mid-October through December 2005, the rapid westward migration of spine 6 slowed and vertical growth of another spine (spine 7) became notable (fig. 7; supplemental movie).

Rates of extrusion and associated motion of assorted segments of the 2004–5 lava dome varied in time and space, but for extended periods extrusion occurred at nearly steady rates. The average rate of vertical displacement varied between about 1 and 4 m/d, with a central tendency toward 2–3 m/d from November 2004 through June 2005 during growth of spines 3, 4, and 5 (fig. 8*A*). From about late June to mid-July 2005, the rate of vertical displacement of spine 5 slowed substantially, then increased from mid- to late July during a period of reinvigorated growth. Following a series of rockfalls in late July, vertical motion of spine 5 diminished, but another, though less vigorous, growth spurt occurred in early to mid-August as spine 6 emerged. In December 2005 the average vertical motion of spine 7 hovered around 1 m/d (fig. 8*A*). In contrast, the average rate of horizontal displacement (in the focal plane) during emplacement of recumbent spines 3 and

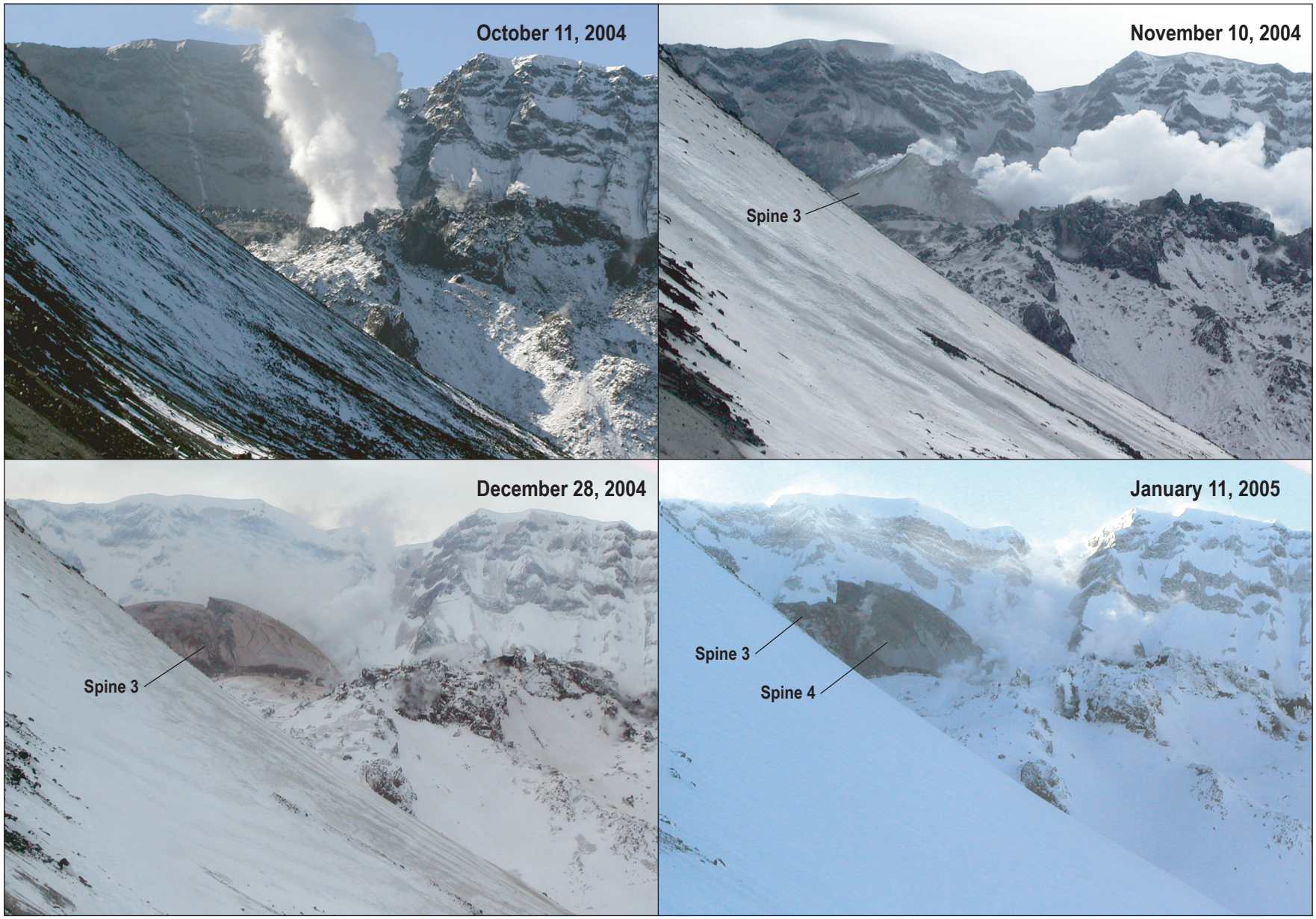

Figure 7. Time series of images from the Sugar Bowl camera illustrating growth, disintegration, and morphologic change of the new lava dome at Mount St. Helens between October 2004 and January 2006.

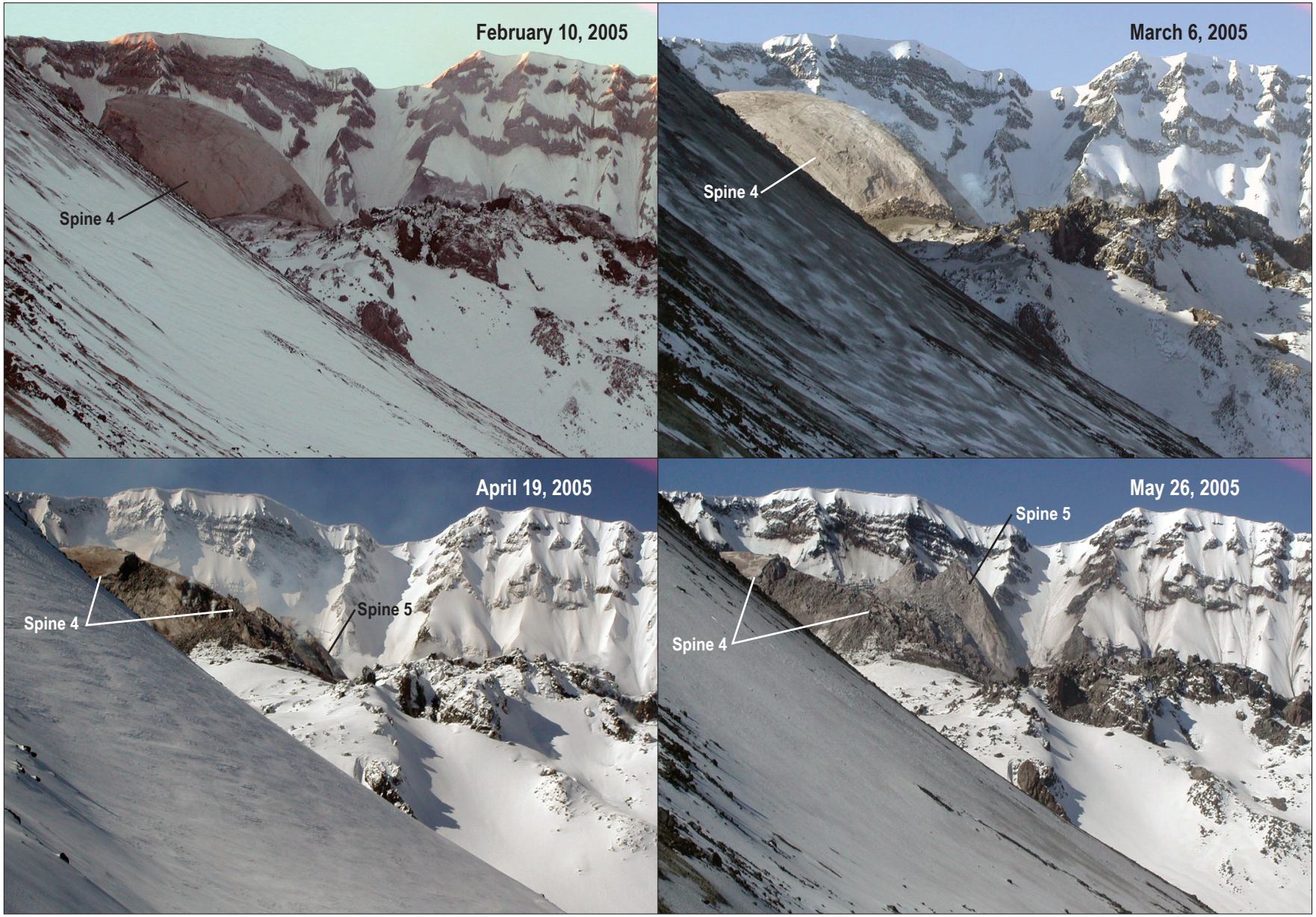

Figure 7.—Continued.

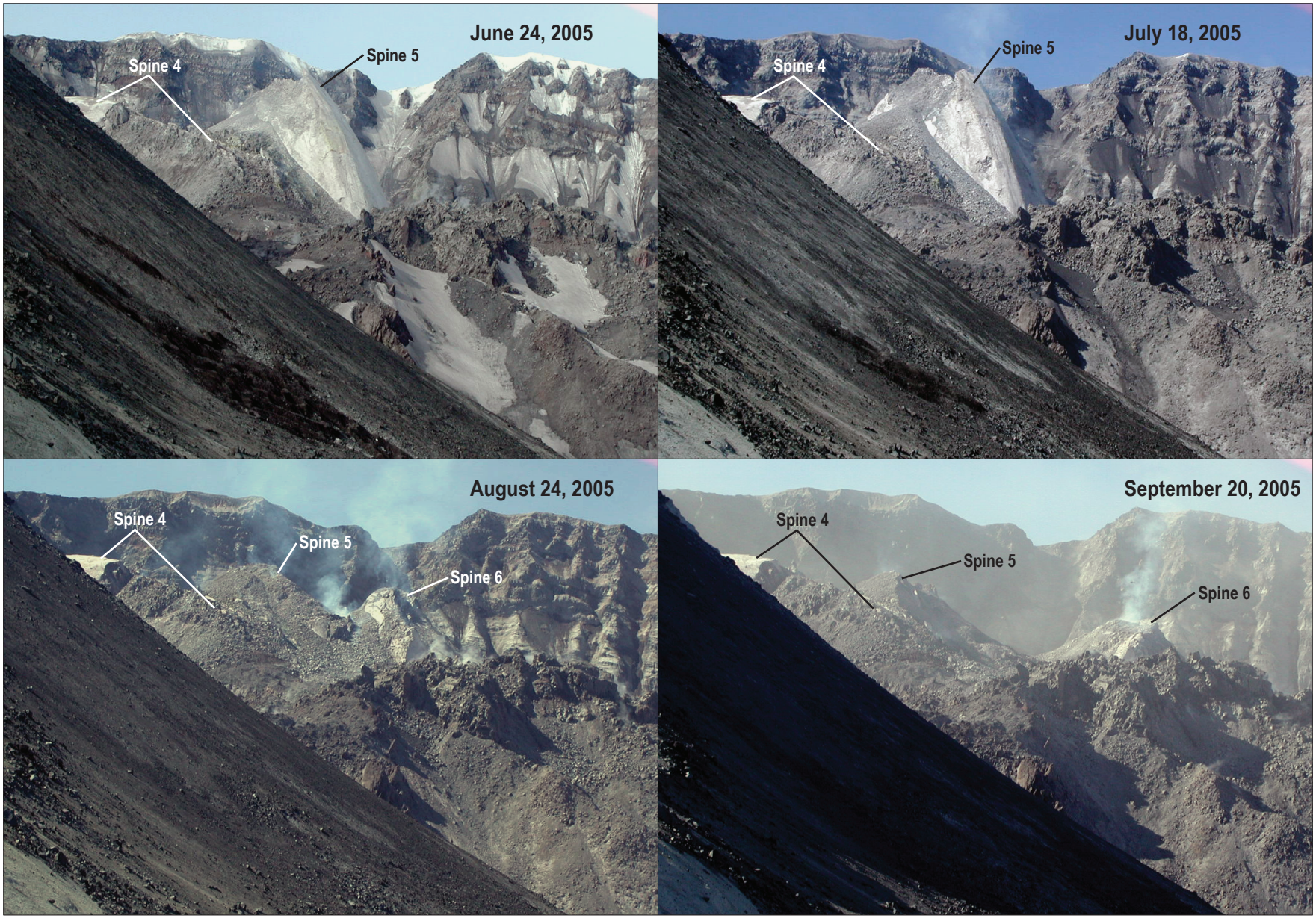

Figure 7.—Continued.

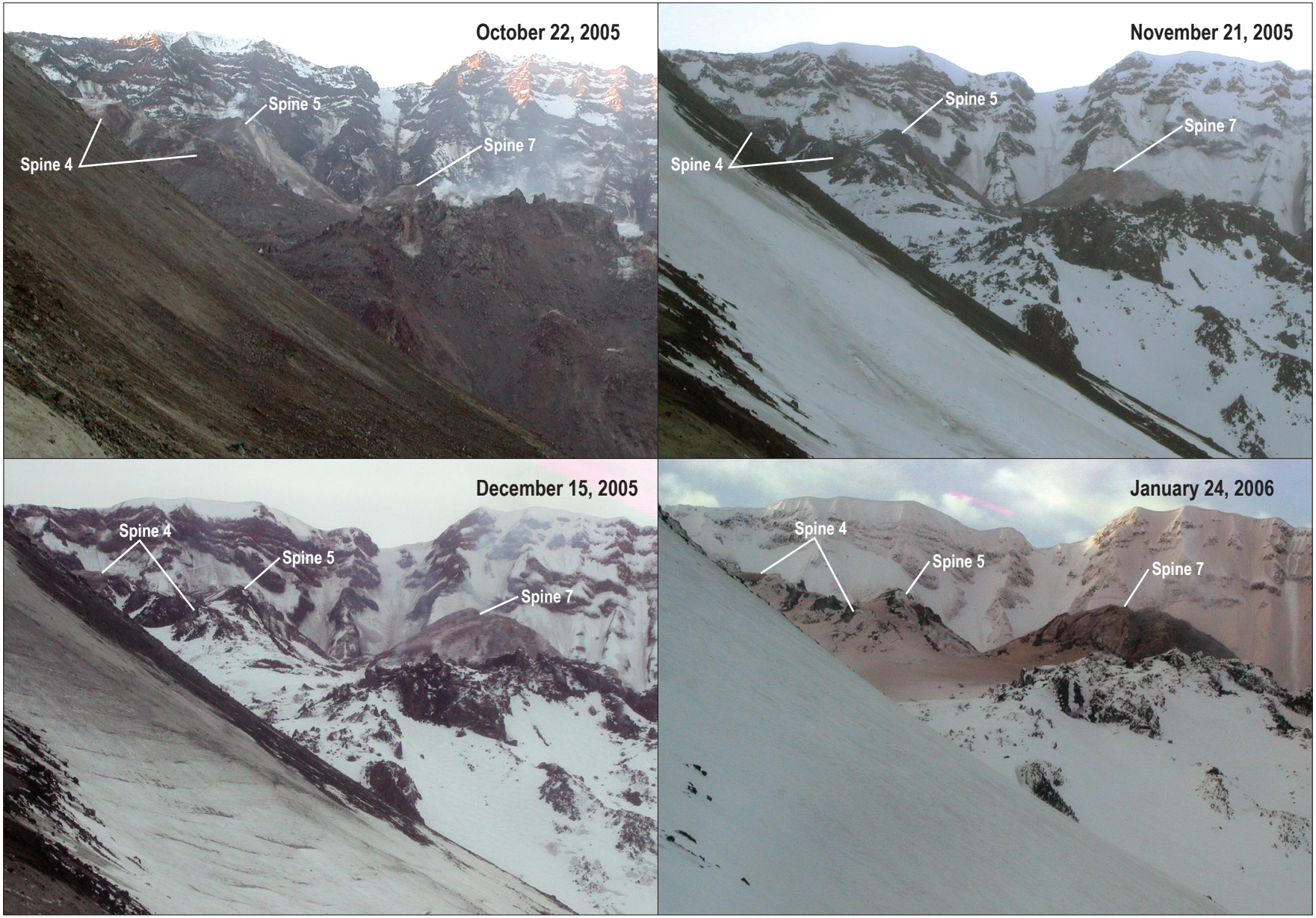

Figure 7.—Continued.

4 decreased progressively from about 5–7 m/d in November 2004 to about 3 m/d by mid-March 2005, then to fractions of a meter per day by late July 2005 after vertical growth of spine 5 became predominant (fig. 8*B*). Horizontal motion increased substantially in August (to >2 m/d) when growth of spine 6 migrated sharply westward; in December 2005, apparent horizontal motion of spine 7 hovered around 2 m/d.

Resolving the average horizontal and vertical displacement rates of the various spines into average rates of motion in the focal plane and then correcting those measurements for the angle of obliquity of extrusion shows that estimated extrusion rates declined logarithmically from November 2004 through December 2005 (fig. 8*C*). This decline is comparable to changes in magma discharge documented through analyses of DEMs (Schilling and others, this volume, chap. 8). However, several spurts of accelerated extrusion are superposed on the overall diminishing extrusion rate, and for several months lava extruded at a nearly steady rate (fig. 8*C*).

The estimated average linear extrusion rate was as great as 8–10 m/d in early November 2004 during emplacement of spine 3, hovered between 4 and 5 m/d from late December 2004 through mid-March 2005 during growth of spine 4, dropped to less than 2 m/d by mid-July 2005 during the waning stages of growth of spine 5, and then increased to about 4 m/d before spine 5 disintegrated in late July 2005. Following disintegration of spine 5, the extrusion rate again dropped to as low as 2 m/d before accelerating to about 4 m/d in August, when spine 6 emerged and migrated sharply westward. In December 2005, during growth of spine 7, the extrusion rate had again declined to about 2 m/d. GPS receivers deployed on spines 3 and 4 tracked extrusion rates in real time for limited periods (LaHusen and others, this volume, chap. 16). During the periods when usable imagery and GPS deployment coincided, estimates of extrusion rate compiled from imagery analyses are about 20–30 percent lower than the measured rates (fig. 8*C*). Given the assumptions in our analyses, our estimates of linear extrusion rate compare relatively favorably with measured rates.

Motion of the extruded lava varied spatially as well as temporally. Movement of the distal ends of recumbent spines 3 and 4 slowed as those spines enlarged, plowed over fragments of earlier spines, and impinged upon the crater wall. Differential rates of motion between distal and near-vent segments of those spines prompted development of thrust faults, large-scale fractures, and partial to complete disintegration in December 2004, January 2005, and April 2005 (fig. 7; supplemental movie; Schilling and others, this volume, chap. 8; Vallance and others, this volume, chap. 9). Such disintegration generated hot rockfalls and minor pyroclastic surges but did not trigger substantive pyroclastic flows similar to those produced by dome collapses elsewhere (for example, Ui and others, 1999; Herd and others, 2005). Following the disintegration of spine 4 (the largest of the recumbent spines) in mid-April 2005, the growth of spine 5 became focused along the western margin of the dome complex. During this phase of growth, active extrusion was effectively decoupled from the remnants of the earlier spines. From mid-April on, several remnants of spines 3 and 4 remained stable as spine 5 emerged (for example, note the stability of the intact block of spine 4 on the east margin of the dome complex between April and December 2005; fig. 7; supplemental movie). Local displacement of ground near the vent, however, showed that, on occasion, extruding solidified lava was well coupled to the immediately surrounding terrain (see supplemental movie).

Following the disintegration of spine 5 in July 2005, the dome became further segmented. As spine 6 emerged and migrated westward, the eastern segment of the dome complex remained stable, but the central segment slumped as its westward buttress was removed (fig. 7; supplemental movie). Such spatially differential motion and migration of the extruding solidified lava led to the segmented morphology of the 2004–5 dome (fig. 9), in contrast to the composite, but uniform morphology of the 1980s lava dome (see, for example, Swanson and others, 1987).

Extrusion rates estimated from the Sugar Bowl imagery are broadly correlated with overall trends in seismicity and deformation (fig. 10). From November 2004 until January 2005, the rapidly decreasing extrusion rate was synchronous with a general decline in seismic-energy release as indicated by real-time seismic amplitude measurements (RSAM) (Endo and Murray, 1991; Murray and Endo, 1992; Moran and others, this volume, chap. 2) (figs. 10*A*, *C*). The RSAM values are commonly invoked as a proxy highlighting overall seismic-energy release at volcanoes (for example, Power and others, 1994, 1995; Harlow and others, 1996; Mori and others, 1996; Voight and others, 1998). During phases of more or less steady extrusion from January to June 2005, minor increases in extrusion rate generally correlated with slight increases in RSAM. The extrusion-rate nadir and subsequent significant growth spurt in mid- to late July 2005 correspond with an equivalent nadir and subsequent minor increase in RSAM.

Correlations between trends in extrusion rate and geodetic measurements of deformation of a part of the 1980s lava dome are evident, but they are more subtle than are those with trends in seismicity (figs. 10*B*, *C*). We compare trends in extrusion rate with trends in the motion of station DOM1 located on the west side of the 1980s lava dome north-northwest of the vent of the 2004–5 eruption (Dzurisin and others, this volume, chap. 14; LaHusen and others, this volume, chap. 16). The overall logarithmic decay of the rate of lava extrusion is approximately mimicked by a corresponding logarithmic change in the northing component of motion of DOM1. Finer scale fluctuations in lava extrusion rate and motion of DOM1 are, however, typically out of phase, particularly after about the first 5 months of the eruption. For example, an increase in extrusion rate between late April and mid-June 2005 corresponds with southward movement of DOM1 (that is, a relaxation of the 1980s dome toward the 2004–5 vent). From late June through mid-July 2005, an ensuing period of declining extrusion rate corresponds with a period of increased northward movement of DOM1 (that is, movement of the 1980s dome away from the vent). An ensuing increase of extrusion

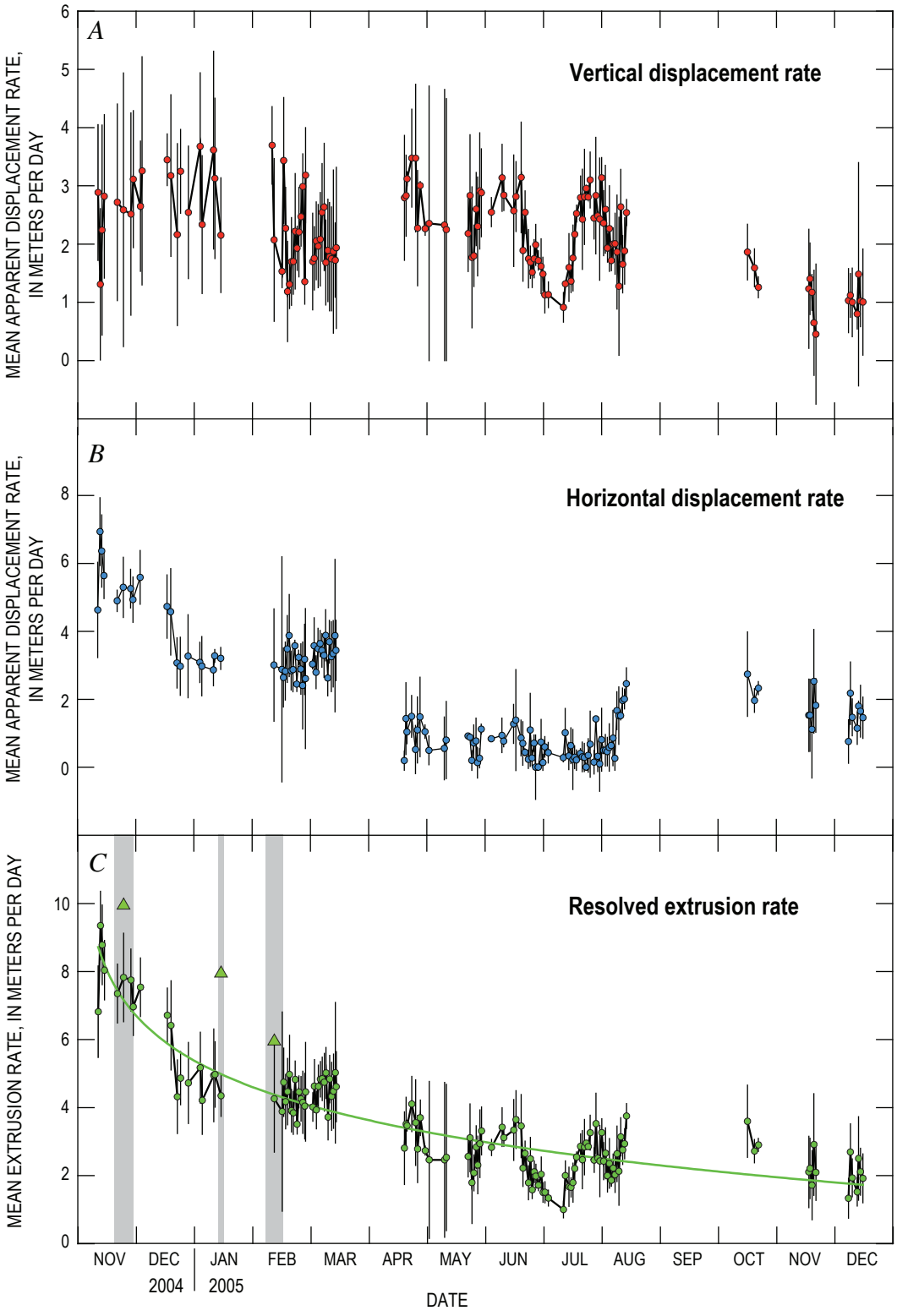

Figure 8. Time-series plot of displacement rates and extrusion rates of the 2004–5 lava dome at Mount St. Helens. Error bars represent ±1 standard deviation about the mean. *A*, Average rate of vertical displacement within the camera focal plane. *B*, Average rate of horizontal displacement within the camera focal plane. *C*, Estimated average extrusion rate of the 2004–5 lava dome in the direction of growth. The gray bands illustrate periods when GPS receivers were deployed on the lava dome, and the triangles represent the average rates of motion measured by GPS (LaHusen and others, this volume, chap. 16). A logarithmic decay curve is superposed on the data.

rate in late July again corresponds with southward movement of DOM1 (toward the vent), whereas the decrease of extrusion rate in early August corresponds with increased northward motion of DOM1 (again, away from the vent). The increase of extrusion rate documented in mid-August 2005 is not as well out of phase with the motion of DOM1 as are other periods of changing rates of extrusion, but it does correspond to a gradual change from northward motion (away from the vent) to southward motion (toward the vent). Only the northing component of motion of DOM1 appears to broadly correspond with variations in extrusion rate; there is little if any substantive correlation between extrusion rate and the easting or vertical components of motion of DOM1 (figs. 10*B*, *C*).

Discussion

Within the constraints of the interior and exterior control we imposed, the available oblique, terrestrial imagery from the Sugar Bowl camera provided a valuable means of estimating long-term linear extrusion rates over periods of weeks to months during the 2004–5 eruption of Mount St. Helens. The greatest sources of error revolved around our assumptions regarding the camera focal length and our ability to accurately coregister sequential images and follow features of interest through time. Pitting of the glass on the camera box, shadows, steam and clouds, weather-related loss of usable images, and physical changes to the dome during its growth and partial disintegration all contributed to the challenge of using the imagery. Although the locus of extrusion varied slightly during the period of analysis, errors in the imposed external control and measurements of the distance between the camera and the dome were relatively small compared to other sources of error. Indeed, the errors associated with the assumed focal length alone make the greatest difference in our comparisons of extracted versus measured extrusion rates.

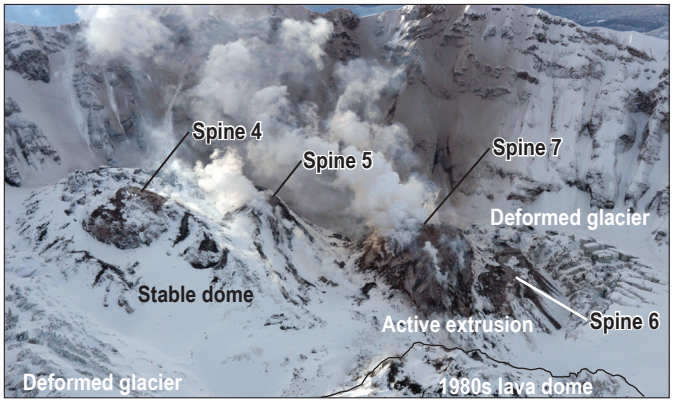

Figure 9. Oblique aerial photograph looking southwest into the crater of Mount St. Helens. Photograph illustrates the segmented morphology of the 2004–5 lava dome complex. Remnants of spines 4 and 5 are visible as discrete snowclad humps on the left and left-center of the image, and the locus of active growth, spine 7, is visible on the right side of the image. Fractured and deformed glacier ice is visible on the far left and far right sides of the image, and part of the snow-covered 1980s lava dome is visible in the bottom center of the image. USGS photograph by J.S. Pallister, December 6, 2005.

Our methodology for extracting quantitative information from the fixed-position imagery hinged upon an ability to impose external control. In the absence of a time series of DEMs, or even a single DEM, we would not have been able to solve the underdetermined system of equations posed by having imagery from only a single viewpoint. Traditional surveying could have provided the necessary measures of distance from the camera site to the dome, but the dangerous environment in the crater during the early phases of the eruption, the distance between the camera and the lava dome, the difficulty of precisely placing prisms even remotely, and the rapidly changing physical character of the dome inhibited such a strategy.

The ability to quantify the rate of extrusion, even crudely, greatly enhanced the value of the imagery. Rather than simply serving as a method to monitor the status of the eruption or the conditions in the crater, the imagery supplemented other geophysical monitoring equipment. For the most part, it provided the sole means of extracting long-term, semicontinuous quantitative information. Differencing of sequential DEMs provided long-term estimates of magma discharge (Schilling and others, this volume, chap. 8), but those DEMs were based on stereoscopic aerial photographs only acquired about once per month. Hence, DEM differencing could not provide information on the fine-scale fluctuations of extrusion rate apparent in the camera imagery. Thus, quantification of linear extrusion rate of the lava from the Sugar Bowl imagery provided information about the eruption that was unattainable by other means.

Deployment of remote cameras at Mount St. Helens clearly enhanced documentation and analysis of the eruption (Poland and others, this volume, chap. 11). The semicontinuous imagery obtained from the Sugar Bowl camera was particularly useful for analyzing long-term, relatively fine-scale (days to months) variations of the linear extrusion rate. It proved less useful for examining extrusion rate over periods of hours, given the low average rates of movement, the challenges of accurately following features of interest, and the resolution of the pixel footprint at the distances involved. Hence, the scale of the imagery had a direct bearing on the quality and utility of the information that could be extracted. Finer resolution at shorter time scales requires more narrowly focused, larger scale imagery, but obtaining such imagery can be extremely challenging (Dzurisin and others, this volume, chap. 14). Of course, measurements of linear extrusion rate do not necessarily correlate directly with measurements of volumetric extrusion rate (that is, magma discharge). Nevertheless, long-term estimates and documentation of fluctuations of this one-dimensional parameter are useful and shed insights

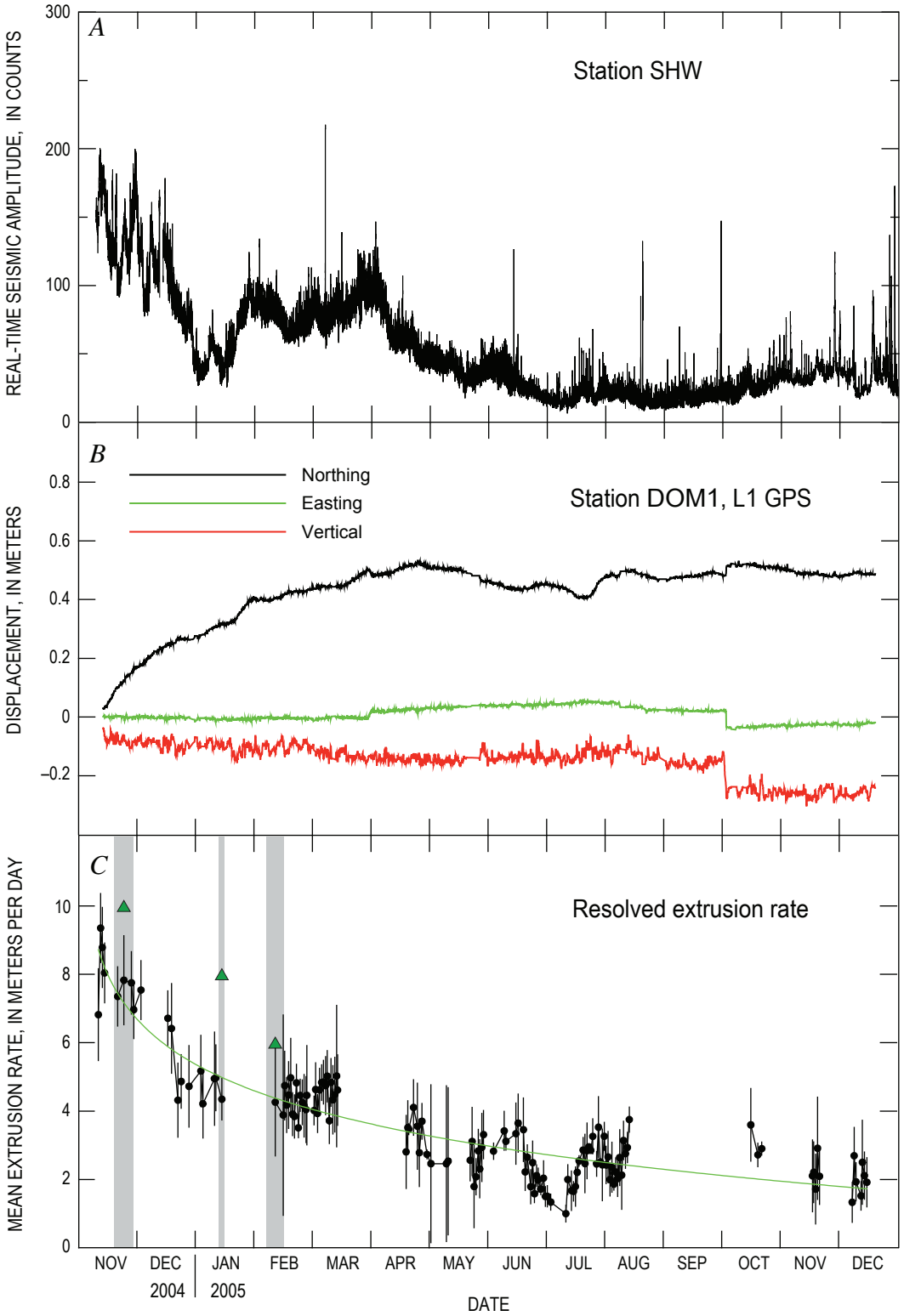

Figure 10. Time-series plots of RSAM, geodetic measurements, and extrusion rate at Mount St. Helens. *A*, Real-time seismic-amplitude measurements (RSAM) from station SHW located on the west flank of the volcano. Plot has been smoothed using a five-point moving average. *B*, GPS geodetic measurements at station DOM1 located on the western side of the 1980s lava dome. The data, obtained using the L1-band frequency, are referenced relative to a station located in the upper South Fork Toutle River valley (LaHusen and others, this volume, chap. 16). Plot has been smoothed using an 11-point moving median. *C*, Estimated average extrusion rate of the 2004–5 lava dome. See figure caption 8*C* for details.

into overall eruptive behavior, especially when trends in linear extrusion rate can be correlated with trends in other geophysical measurements.

The pulsating behavior of lava extrusion documented on time scales of days to weeks in our analysis has been observed on time scales of hours to years during emplacement of other silicic lava domes. At Soufrière Hills volcano, Montserrat, West Indies, Sparks and others (1998) noted that magma discharge pulsated on time scales of hours to months during a time when the overall discharge rate was increasing. In contrast, the pulsating behavior documented here occurred during an overall trend of declining magma discharge (Schilling and others, this volume, chap. 8). Fluctuating extrusion rates during an overall decline of magma discharge were also observed at Unzen volcano, Japan, from 1991 to 1995 (Nakada and others, 1999). Lava at Santiaguito dome, Guatemala, has extruded continuously since 1922, with 3–5-yr spurts of rapid discharge interspersed with 10–15-yr periods of slower discharge (Rose, 1987; Anderson and others, 1995; Harris and others, 2003). The Mount St. Helens 1980–86 lava dome grew through a series of 20 eruptive episodes between October 1980 and October 1986. However, each discrete extrusive episode was separated by pauses in eruptive activity that ranged from about one month to one year (Swanson and others, 1987), in contrast to the sustained, but fluctuating, extrusion that characterized the 2004–5 eruption. Sparks and others (1998) attribute pulsating extrusive behavior to a combination of deep and shallow volcanic processes. They speculate that discharge fluctuations on time scales of months to years are influenced chiefly by deep processes that control magmatic influx from the mantle and magma-chamber processes that affect magma ascent. In contrast, fluctuations on time scales of hours to weeks are attributed chiefly to pressure fluctuations caused by shallow-level processes, such as gas loss, crystallization kinetics, and mineral precipitation, which affect changes in magma properties and pressurization.

Correlations among seismicity, deformation, and extrusion rate during the 2004–5 Mount St. Helens eruption portray an extrusion that likely consisted of episodes of broad-scale stick-slip behavior. Relatively fine-scale correlations among periods of declining extrusion rate, relatively low seismicity, and northward movement of the 1980s lava dome (away from the eruptive vent) suggest episodes when the extruding solidified plug of lava was relatively well coupled to, and having difficulty evacuating, the conduit. Such a period of "stick" would be expected to result in lower seismicity, a low rate of extrusion, and increased deformation (that is, swelling) of the local terrain. In contrast, broad correlation among accelerated extrusion rate, slightly elevated seismicity, and southward movement of the 1980s lava dome (toward the eruptive vent) suggest episodes when the extruding solidified lava was relatively poorly coupled to, and slipping through, the conduit. Such periods of "slip" generated more or larger earthquakes as the lava dome lurched along (Moran and others, this volume, chap. 2) and allowed the local terrain deformed during the preceding period of stick to relax. Such episodes of broad-scale stick-slip movement complement a dynamic model of repetitive, fine-scale, stick-slip movement during sustained extrusion as proposed by Iverson and others (2006) and Iverson (this volume, chap. 21).

Long-term (months) and short-term (days) correlations between seismic intensity, deformation, and dome growth, such as documented here, have also been noted at other volcanoes. Broad correlations between seismic intensity and dome growth have been documented at Usu (Wano and Okada, 1980), Augustine (Power, 1988), Redoubt (Power and others, 1994), Unzen (Nakada and others, 1999), and Montserrat (Rowe and others, 2004), and short-term synchronicity and cyclicity between seismicity and deformation also have been observed (Voight and others, 1998). However, long-term, fine-scale correlations among fluctuations in extrusion rate, seismicity, and deformation generally have not been reported. Such correlations, as noted above, are clearly related to eruption mechanics. Indeed, Denlinger and Hoblitt (1999) have modeled short-term synchronicity and cyclicity in RSAM and deformation at Montserrat as a function of the interaction of volatile overpressure in magma and the overburden of an extruding lava dome, and Iverson (this volume, chap. 21) has hypothesized that the small, repetitive earthquakes that have occurred during the 2004–5 Mount St. Helens eruption, dubbed drumbeat earthquakes (Moran and others, this volume, chap. 2), reflect repetitive, small-magnitude (a few millimeters) stick-slip behavior of the extruding lava. Extraction of semicontinuous extrusion rates from long-term camera imagery, in conjunction with time-series of other geophysical data, clearly plays an important role in constraining dynamic eruption models and enabling forecasts of hazardous activity.

Conclusions

Imposition of interior and exterior controls on a semicontinuous series of oblique, terrestrial imagery from a fixed vantage point on the Sugar Bowl lava dome allowed quantification of fine-scale temporal behavior of the linear rate of lava extrusion during the 2004–5 eruption of Mount St. Helens. Analysis of the imagery showed that over a period of 14 months (November 2004–December 2005), the linear extrusion rate varied in both space and time. Overall, the extrusion rate declined approximately logarithmically from about 8–10 m/d in November 2004 to about 2 m/d by December 2005. However, the overall decline in the rate of extrusion was punctuated by fine-scale (days to weeks) fluctuations. The overall logarithmic decline of extrusion rate and the finer scale fluctuations correlated, approximately, with trends in seismicity and geodetic deformation. Those correlations portray an extrusion that underwent episodes of broad-scale stick-slip movement in addition to finer scale, smaller magnitude stick-slip episodes that others hypothesize to correlate with small, so-called drumbeat earthquakes. The ability to extract linear

extrusion rates from the imagery from this fixed-position camera provided a significant, and sometimes the sole, means of semicontinuously quantifying eruption dynamics during much of the first year of eruption, and those data provide an important constraint for dynamic eruption models.

Acknowledgments

As noted in this chapter, the Sugar Bowl camera was not specifically deployed with the intention of extracting quantitative information. However, when viewing the images, especially after they have been compiled into a time-lapse movie, one cannot help but realize that they contain a plethora of information about the growth, and the rate of growth, of the new lava dome. The trick is to extract that information. We thank our colleagues at the Hawaiian Volcano Observatory for providing us with the original camera and communications software; Gene Iwatsubo, Kirstie Simpson, and Stephanie Konfal for helping install the camera; Seth Moran for providing us with RSAM data; Steve Schilling for stimulating discussions as we muddled along through our analyses; Matt Logan and Dan Gooding for compiling the imagery into the movie included in the supplemental movie of appendix 1; our many colleagues at CVO who asked pointed questions at staff meetings when we unveiled our analyses; and Ren Thompson and Ricky Herd for insightful, critical reviews that kept us from wandering beyond the limits of what we could reasonably do in our efforts to extract information from these photographs.

References Cited

Anderson, S.W., Fink, J.H., and Rose, W.I., 1995, Mount St. Helens and Santiaguito lava domes; the effect of short-term eruption rate on surface texture and degassing processes: Journal of Volcanology and Geothermal Research, v. 69, p. 105–116.

Baldi, P., Bonvalot, S., Briole, P., and Marsella, M., 2000, Digital photogrammetry and kinematic GPS applied to the monitoring of Vulcano Island, Aeolian arc, Italy: Geophysics Journal International, v. 142, no. 3, p. 801–811.

Baldi, P., Fabris, M., Marsella, M., and Monticelli, R., 2005, Monitoring the morphological evolution of the Sciara del Fuoco during the 2002–2003 Stromboli eruption using multi-temporal photogrammetry: ISPRS Journal of Photogrammetry and Remote Sensing, v. 59, no. 4, p. 199–211.

Barmin, A., Melnik, O., and Sparks, R.S.J., 2002, Periodic behavior in lava dome eruptions: Earth and Planetary Science Letters, v. 199, p. 173–184.

Bevington, P.R., and Robinson, D.K., 1992, Data reduction and error analysis for the physical sciences (2d ed.): Boston, McGraw-Hill, 328 p.

Denlinger, R.P., and Hoblitt, R.P., 1999, Cyclic eruptive behavior of silicic volcanoes: Geology, v. 27, p. 459–462.

Dungan, M.A., Wulff, A., and Thompson, R.A., 2001, Eruptive stratigraphy of the Tatara-San Pedro complex, 36°S, Southern Volcanic Zone, Chilean Andes; reconstruction method and implications for magma evolution at long-lived arc volcanic centers: Journal of Petrology, v. 42, p. 555–626.

Dzurisin, D., Lisowski, M., Poland, M.P., Sherrod, D.R., and LaHusen, R.G., 2008, Constraints and conundrums resulting from ground-deformation measurements made during the 2004–2005 dome-building eruption of Mount St. Helens, Washington, chap. 14 *of* Sherrod, D.R., Scott, W.E., and Stauffer, P.H., eds., A volcano rekindled; the renewed eruption of Mount St. Helens, 2004–2006: U.S. Geological Survey Professional Paper 1750 (this volume).

Endo, E.T., and Murray, T., 1991, Real-time seismic amplitude measurement (RSAM); a volcano monitoring and prediction tool: Bulletin of Volcanology, v. 53, no. 7, p. 533–545.

Harlow, D.H., Power, J.A., Laguerta, E.P., Ambubuyog, G., White, R.A., and Hoblitt, R.P., 1996, Precursory seismicity and forecasting of the June 15, 1991 eruption of Mount Pinatubo, *in* Newhall, C.G., and Punongbayan, R.S., eds., Fire and mud; eruptions and lahars of Mount Pinatubo, Philippines: Seattle, University of Washington Press, p. 285–305.

Harris, A.J.L., Rose, W.I., and Flynn, L.P., 2003, Temporal trends in lava dome extrusion at Santiaguito 1992–2000: Bulletin of Volcanology, v. 65, p. 77–89.

Herd, R.A., Edmonds, M., and Bass, V.A., 2005, Catastrophic lava dome failure at Soufriere Hills Volcano, Montserrat, 12–13 July 2003: Journal of Volcanology and Geothermal Research, v. 148, nos. 3–4, p. 234–252, doi:10.1016/j.jvolgeores.2005.05.003.

Honda, K., and Nagai, M., 2002, Real-time volcano activity mapping using ground-based digital imagery: ISPRS Journal of Photogrammetry and Remote Sensing, v. 57, p. 159–168.

Huppert, H.E., Shepherd, J.B., Sigurdsson, H., and Sparks, R.S.J., 1982, On lava dome growth, with application to the 1979 lava extrusion of the Soufrière of St. Vincent: Journal of Volcanology and Geothermal Research, v. 14, p. 199–222.

Iverson, R.M., 2008, Dynamics of seismogenic volcanic extrusion resisted by a solid surface plug, Mount St. Helens, 2004–2005, chap. 21 *of* Sherrod, D.R., Scott, W.E., and Stauffer, P.H., eds., A volcano rekindled; the renewed eruption of Mount St. Helens, 2004–2006: U.S. Geological Survey Professional Paper 1750 (this volume).

Iverson, R.M., Dzurisin, D., Gardner, C.A., Gerlach, T.M., LaHusen, R.G., Lisowski, M., Major, J.J., Malone, S.D., Messerich, J.A., Moran, S.C., Pallister, J.S., Qamar, A.I., Schilling, S.P., and Vallance, J.W., 2006, Dynamics of seismogenic volcanic extrusion at Mount St. Helens in 2004–05: Nature, v. 444, no. 7118, p. 439–443, doi:10.1038/nature05322.

James, M.R., Robson, S., Pinkerton, H., and Ball, M., 2006, Oblique photogrammetry with visible and thermal images of active lava flows: Bulletin of Volcanology, v. 69, no. 1, p. 105–108.

Jordan, R., and Kieffer, H.H., 1981, Topographic changes at Mount St. Helens—large-scale photogrammetry and digital terrain models, *in* Lipman, P.W., and Mullineaux, D.R., eds., The 1980 eruptions of Mount St. Helens, Washington: U.S. Geological Survey Professional Paper 1250, p. 135–141.

LaHusen, R.G., Swinford, K.J., Logan, M., and Lisowski, M., 2008, Instrumentation in remote and dangerous settings; examples using data from GPS "spider" deployments during the 2004–2005 eruption of Mount St. Helens, Washington, chap. 16 *of* Sherrod, D.R., Scott, W.E., and Stauffer, P.H., eds., A volcano rekindled; the renewed eruption of Mount St. Helens, 2004–2006: U.S. Geological Survey Professional Paper 1750 (this volume).

Mastin, L.G., Roeloffs, E., Beeler, N.M., and Quick, J.E., 2008, Constraints on the size, overpressure, and volatile content of the Mount St. Helens magma system from geodetic and dome-growth measurements during the 2004–2006+ eruption, chap. 22 *of* Sherrod, D.R., Scott, W.E., and Stauffer, P.H., eds., A volcano rekindled; the renewed eruption of Mount St. Helens, 2004–2006: U.S. Geological Survey Professional Paper 1750 (this volume).

Melnik, O., and Sparks, R.S.J., 2005, Controls on conduit magma flow dynamics during lava dome building eruptions: Journal of Geophysical Research, v. 110, no. B2, B02209, 21 p., doi:10.1029/2004JB003183.

Molander, C.W., 2001, Photogrammetry, *in* Maune, D.F., ed., Digital elevation model technologies and applications; the DEM users manual: The American Society for Photogrammetry and Remote Sensing, Bethesda, Maryland, p. 121–142.

Moore, J.G., and Albee, W.C., 1981, Topographic and structural changes, March–July 1980—photogrammetric data, *in* Lipman, P.W., and Mullineaux, D.R., eds., The 1980 eruptions of Mount St. Helens, Washington: U.S. Geological Survey Professional Paper 1250, p. 123–134.

Moran, S.C., Malone, S.D., Qamar, A.I., Thelen, W.A., Wright, A.K., and Caplan-Auerbach, J., 2008, Seismicity associated with renewed dome building at Mount St. Helens, 2004–2005, chap. 2 *of* Sherrod, D.R., Scott, W.E., and Stauffer, P.H., eds., A volcano rekindled; the renewed eruption of Mount St. Helens, 2004–2006: U.S. Geological Survey Professional Paper 1750 (this volume).

Mori, J., White, R.A., Harlow, D.H., Okubo, P., Power, J.A., Hoblitt, R.P., Laguerta, E.P., Lanuza, A., and Bautista, B.C., 1996, Volcanic earthquakes following the 1991 climactic eruption of Mount Pinatubo; strong seismicity during a waning eruption, *in* Newhall, C.G., and Punongbayan, R.S., eds., Fire and mud; eruptions and lahars of Mount Pinatubo, Philippines: Seattle, University of Washington Press, p. 339–350.

Murray, T., and Endo, E.T., 1992, A real-time seismic-amplitude measurement system (RSAM), *in* Ewert, J.A., and Swanson, D.A., eds., Monitoring volcanoes; techniques and strategies used by the staff of the Cascades Volcano Observatory, 1980–1990: U.S Geological Survey Bulletin 1966, p. 5–10.

Nakada, S., Miyake, Y., Sato, H., Oshima, O., and Fujinawa, A., 1995, Endogenous growth of dacite dome at Unzen volcano (Japan), 1993–1994: Geology, v. 23, no. 2, p. 157–160.

Nakada, S., Shimizu, H., and Ohta, K., 1999, Overview of the 1990–1995 eruption at Unzen Volcano: Journal of Volcanology and Geothermal Research, v. 89, p. 1–22.

Poland, M.P., Dzurisin, D., LaHusen, R.G., Major, J.J., Lapcewich, D., Endo, E.T., Gooding, D.J., Schilling, S.P., and Janda, C.G., 2008, Remote camera observations of lava dome growth at Mount St. Helens, Washington, October 2004 to February 2006, chap. 11 *of* Sherrod, D.R., Scott, W.E., and Stauffer, P.H., eds., A volcano rekindled; the renewed eruption of Mount St. Helens, 2004–2006: U.S. Geological Survey Professional Paper 1750 (this volume).

Power, J.A., 1988, Seismicity associated with the 1986 eruption of Augustine Volcano, Alaska: Fairbanks, University of Alaska, M.S. thesis, 142 p.

Power, J.A., Lahr, J.C., Page, R.A., Chouet, B.A., Stephens, C.D., Harlow, D.H., Murray, T.L., and Davies, J.N., 1994, Seismic evolution of the 1989–1990 eruption sequence of Redoubt Volcano, Alaska: Journal of Volcanology and Geothermal Research, v. 62, p. 69–94.

Power, J.A., Jolly, A.D., Page, R.A., and McNutt, S.R., 1995, Seismicity and forecasting of the 1992 eruptions of Crater Peak vent, Mount Spurr Volcano, Alaska; an overview, *in* Keith, T.C., ed., The 1992 eruptions of Crater Peak Vent, Mount Spurr Volcano, Alaska: U.S. Geological Survey Bulletin 2139, p. 149–159.

Rose, W.I., 1987, Volcanic activity at Santiaguito volcano, 1976–1984, *in* Fink, J.H., ed., The emplacement of silicic domes and lava flows: Geological Society of America Special Paper 212, p. 17–27.

Rowe, C.A., Thurber, C.H., and White, R.A., 2004, Dome growth behavior at Soufriere Hills Volcano, Montserrat, revealed by relocation of volcanic event swarms, 1995–1996: Journal of Volcanology and Geothermal Research, v. 134, no. 3, p. 199–221.

Schilling, S.P., Carrara, P.E., Thompson, R.A., and Iwatsubo, E.Y., 2004, Posteruption glacier development within the crater of Mount St. Helens, Washington, USA: Quaternary Research, v. 61, no. 3, p. 325–329.

Schilling, S.P., Thompson, R.A., Messerich, J.A., and Iwatsubo, E.Y., 2008, Use of digital aerophotogrammetry to determine rates of lava dome growth, Mount St. Helens, Washington, 2004–2005, chap. 8 *of* Sherrod, D.R., Scott, W.E., and Stauffer, P.H., eds., A volcano rekindled; the renewed eruption of Mount St. Helens, 2004–2006: U.S. Geological Survey Professional Paper 1750 (this volume).

Sparks, R.S.J., and 19 others, 1998, Magma production and growth of the lava dome of the Soufriere Hills Volcano, Montserrat, West Indies—November 1995 to December 1997: Geophysical Research Letters, v. 25, no. 18, p. 3421–3424.

Swanson, D.A., Dzurisin, D., Holcomb, R.T., Iwatsubo, E.Y., Chadwick, W.W., Jr., Casadevall, T.J., Ewert, J.W., and Heliker, C.C., 1987, Growth of the lava dome at Mount St. Helens, Washington (USA), 1981–1983, *in* Fink, J.H., ed., The emplacement of silicic domes and lava flows: Geological Society of America Special Paper 212, p. 1–16.

Thompson, R.A., and Schilling, S.P., 2007, Photogrammetry, *in* Dzurisin, D., ed., Volcano deformation—geodetic monitoring techniques: Berlin, Springer, Springer-Praxis Books in Geophysical Sciences, p. 195–221.

Ui, T., Matsuwo, N., Sumita, M., and Fujinawa, A., 1999, Generation of block and ash flows during the 1990–1995 eruption of Unzen volcano, Japan: Journal of Volcanology and Geothermal Research, v. 89, p. 123–137.

Vallance, J.W., Schneider, D.J., and Schilling, S.P., 2008, Growth of the 2004–2006 lava-dome complex at Mount St. Helens, Washington, chap. 9 *of* Sherrod, D.R., Scott, W.E., and Stauffer, P.H., eds., A volcano rekindled; the renewed eruption of Mount St. Helens, 2004–2006: U.S. Geological Survey Professional Paper 1750 (this volume).

Voight, B., 1981, Time scale for the first moments of the May 18 eruption, *in* Lipman, P.W., and Mullineaux, D.R., eds., The 1980 eruptions of Mount St. Helens, Washington: U.S. Geological Survey Professional Paper 1250, p. 69–86.

Voight, B., Hoblitt, R.P., Clarke, A.B., Lockhart, A.B., Miller, A.D., Lynch, L.L., and McMahon, J., 1998, Remarkable cyclic ground deformation monitored in real time on Montserrat, and its use in eruption forecasting: Geophysical Research Letters, v. 25, p. 3405–3408.

Wano, K., and Okada, H., 1980, Peculiar occurrence of Usu earthquake swarms associated with recent doming activity: Jishin, v. 33, p. 215–226.

Wolf, P.R., and Dewitt, B.A., 2000, Elements of photogrammetry with applications in GIS (3d ed.): Boston, McGraw-Hill, 608 p.

Yamashina, K., Matsushima, T., and Ohmi, S., 1999, Volcanic deformation at Unzen, Japan, visualized by a time-differential stereoscopy: Journal of Volcanology and Geothermal Research, v. 89, p. 73–80.

Zlotnicki, J., Ruegg, J.C., Bachelery, P., and Blum, P.A., 1990, Eruptive mechanism on Piton de la Fournaise volcano associated with the December 4, 1983, and January 18, 1984 eruptions from ground deformation monitoring and photogrammetric surveys: Journal of Volcanology and Geothermal Research, v. 40, no. 3, p. 197–217, doi:10.1016/0377-0273(90)90121-U.

Appendix 1. Time-Lapse Photography of Mount St. Helens, 2004–2006—Movie

[This appendix appears only in the digital versions of this work in the DVD-ROM that accompanies the printed volume and as a separate file accompanying this chapter on the Web at: http://pubs.usgs.gov/pp/1750.]

The appendix is a time-lapse movie showing dome growth at Mount St. Helens from November 10, 2004, to May 10, 2006. The movie, in mpeg-1 file format and titled “Sugarbowl to May10 2006_5000.mpg,” is composed of 188 photographs taken by the Sugar Bowl remote camera. It was assembled by choosing the best image per day for times when weather was suitable for viewing the dome. File size is 23 Mb. Compiled by Matt Logan and Dan Gooding (USGS).